Photothermal spectro-microscopy as benchmark for optoplasmonic bio-detection assays

Baaske, M.D.; Asgari, N.; Späth, P.R.; Adhikari, S.; Punj, D.; Orrit, M.A.G.J.

THE JOURNAL OF PHYSICAL CHEMISTRY C
A JOURNAL OF THE AMERICAN CHEMICAL SOCIETY

pubs.acs.org/JPCC

Article

Photothermal Spectro-Microscopy as Benchmark for Optoplasmonic Bio-Detection Assays

Published as part of The Journal of Physical Chemistry virtual special issue "W. E. Moerner Festschrift".

Martin. D. Baaske, Nasrin Asgari, Patrick Spaeth, Subhasis Adhikari, Deep Punj, and Michel Orrit*

Cite This: *J. Phys. Chem. C* 2021, 125, 25087−25093

Read Online

ACCESS | Metrics & More | Article Recommendations

ABSTRACT: Optoplasmonic bio-detection assays commonly probe the response of plasmonic nanostructures to changes in their dielectric environment. The accurate detection of nanoscale entities such as virus particles, micelles and proteins requires optimization of multiple experimental parameters. Performing such optimization directly via analyte recognition is often not desirable or feasible, especially if the nanostructures exhibit limited numbers of analyte binding sites and if binding is irreversible. Here we introduce photothermal spectro-microscopy as a benchmarking tool for the characterization and optimization of optoplasmonic detection assays.

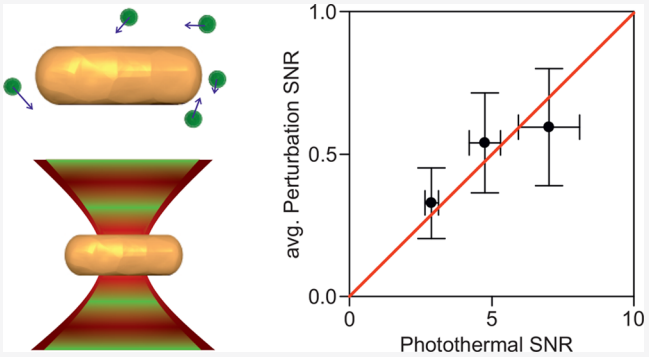

INTRODUCTION

Individual (bio)molecules can be detected optically through their fluorescence,[1] absorption,[2] or mere refraction.[3] Optoplasmonic methods, which harness strong near fields around plasmonic metal nanostructures to enhance the sensitivity and selectivity of optical detection, have evolved over the past decade into powerful tools for biomolecular recognition. Dedicated versions of these methods now enable the detection of a wide range of molecules and nanoparticles, on a single-object basis.[4−12] Sensitive refractometric sensors such as optical microresonators also provide powerful platforms for molecular recognition,[13,14] especially in combination with plasmonic particles.[15−21] At the same time novel microscopic methods make use of plasmonic particles as photostable labels[22,23] and combine them with optical, electromagnetic, or electric devices for trapping and manipulation of sensor particles or even of the molecules themselves.[24−29] In the following we will exclusively focus on optoplasmonic assays that facilitate analyte recognition via observation of a plasmonic nanostructure's response to (single) analytes perturbing its dielectric environment. The volume in which such perturbations are recognizable is defined by the extent of the structures' enhanced near-field and is limited to distances on the order of 10 nm away from the structures' surface. Optoplasmonic assays commonly employ specific receptor molecules to bind analytes and to facilitate their detection. These receptors fulfill a dual purpose: (i) They immobilize the analytes inside the detection volume and, thus, provide for long enough integration times required for the detection of the target. (ii) They provide target specificity, as they ideally form sufficiently strong binding exclusively with the targeted molecules. As a consequence, the sensitivity of refractometric optoplasmonic assays depends on two separate factors: (i) The properties of the chemical interface, that is, receptor density, accessibility, and quality; (ii) The properties of the plasmonic structure and the optical interface, that is, spectral quality, spectral position of plasmonic features, structure quality, polarization states, wavelength range, desired bandwidth, type of illumination (widefield or confocal), and the detection electronics. To allow for the consecutive optimization of aspects (i) and (ii), it is desirable to characterize these aspects separately and independently. Here, we show in the example of gold nanorods that photothermal spectro-microscopy provides such a characterization method for plasmonic structures, that is, for aspect (ii).

METHODS

Slide Preparation. Nanorods (NRs) were purchased from Nanopartz. NRs were sonicated for 20 min and then spin-coated onto microscope slides. Next the glass slides were

Received: August 27, 2021
Revised: October 25, 2021
Published: November 9, 2021

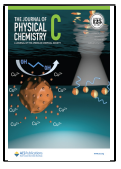

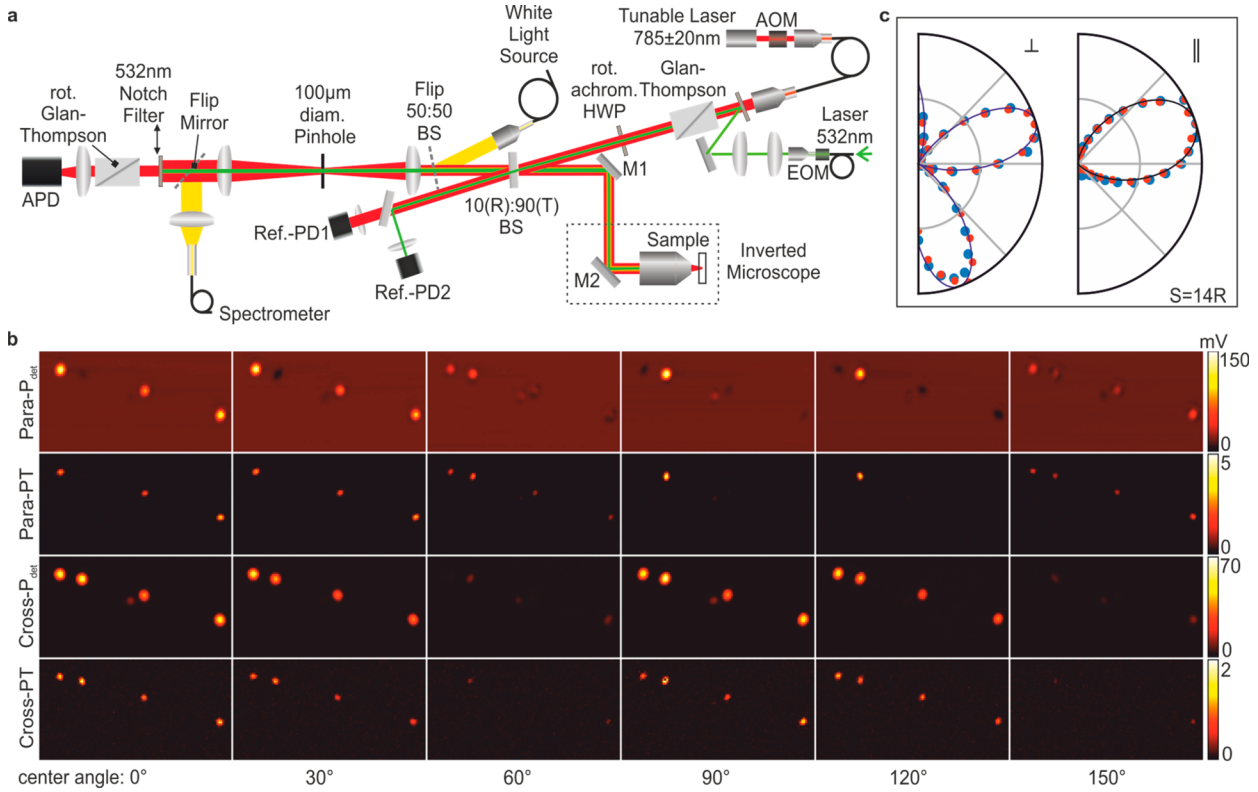

Figure 1. Confocal microscopy setup used for the combined positional, orientational, spectral, and photothermal characterization of single gold nanorods. (b) Confocal scanning images of P_{det} and ΔP_{PT} measured on the same sample area and obtained with crossed (Cross) and parallel (Para) polarizers at different center angles. (c) Angle scans of the same NR with crossed (left) and parallel (right) polarizers: Blue (red) dots mark the P_{det} (ΔP_{PT}) values normalized to their corresponding maximum. Solid lines indicate fits by the theoretical functions.

deposited in a UV-ozone cleaner for 60 min in order to remove residual CTAB and consecutively rinsed with water. Measurements were then performed in glass chambers made from BK-7 and pressed against the slides. Chemicals were purchased from Sigma-Aldrich.

Optical Setup. We used the custom-made confocal setup depicted in Figure 1a. Its components are: Objective: Olympus UPLFLN100XOP; Tube lens: Olympus Super Wide Tube Lens Unit; Lasers: Toptica DL pro 785 nm and Cobolt Samba 532 nm; APD: Thorlabs APD430A/M; 10:90 Beamsplitter BSN11 (Thorlabs); Glan-Thompson Polarizer GTH10M-B (Thorlabs); Piezo Translator P-561.3CD (Physik Instrumente GmbH & Co KG); White-light source: EQ-99XFC (Energetiq); Spectrometer: QE-65000 (Ocean Optics); Reference Photodiodes 1 and 2: PDA36A2 (Thorlabs) and HCA-S-200 M (Femto); EOM: Amplitude Modulator AM532 (Jenoptik); AOM: MT110-A1-IR (AA Opto-Electronic); Achromatic $\lambda/2$ -plate: RAC 4.2.10 (B. Halle); Notch Filter: ZET532NF (Chroma). Data was recorded via an Oscilloscope (WaveSurfer 24MXs-B, Teledyne Lecroy).

RESULTS AND DISCUSSION

Photothermal (PT) microscopy detects a change of optical properties following the absorption of light by an analyte.[2,19,30−36] The dissipation of the absorbed power into the surrounding medium induces a temperature gradient, which modifies the optical properties both of the absorbing objects and of the medium. The associated change of the medium's refractive index notably leads to the formation of a thermal lens.[37,38] Heating-induced changes in the optical properties lead to changes in the scattered light, which are detected as intensity changes of a probe beam illuminating the sample. As these changes are very small, their detection is facilitated if the heating beam's intensity is modulated at a fixed frequency, enabling subsequent phase-sensitive demodulation via a lock-in amplifier which rejects most white and $1/f$ noise. Commonly, the probe beam is used off-resonance so that high probe powers can be used.[2,5,35,37] Here, we deviate from this scheme by probing gold nanorods at wavelengths close to their localized surface plasmon resonance (LSPR), as we are interested in probing their response to heat-induced refractive index changes. We do this with the confocal microscopy setup shown in Figure 1. Specifically, we detect changes in the power P_{det} of the detected probe light, which results from the interference between scattered $E_s \propto \sqrt{S}e^{-i\theta}$ and reflected $E_r \propto \sqrt{R}e^{-i\gamma}$ electric fields: $P_{det} \propto (E_s + E_r)(E_s + E_r)^* \propto R + 2\eta\sqrt{SR}\cos\phi + S$, where * denotes the complex conjugate, and R and S are the effective reflection coefficient and scattering cross section, respectively. Further, $\phi = \theta - \gamma$ denotes the phase difference between the reflected and the scattered field, where γ is the Gouy phase and θ is the phase difference between incident and scattered field. Both S and θ depend on the frequency detuning of the probe laser's frequency ν with respect to the resonance frequency of the NR's LSPR-frequency, ν_{LSPR}. The factor η denotes the mode-matching efficiency between scattered and reflected fields. Changes in the NR's dielectric environment give rise to a change ΔS of the NR's scattering cross section at the probe wavelength as well as a change in the phase difference between scattered and reflected light $\Delta(\cos\phi)$ due to the shift of the LSPR

https://doi.org/10.1021/acs.jpcc.1c07592
J. Phys. Chem. C 2021, 125, 25087−25093

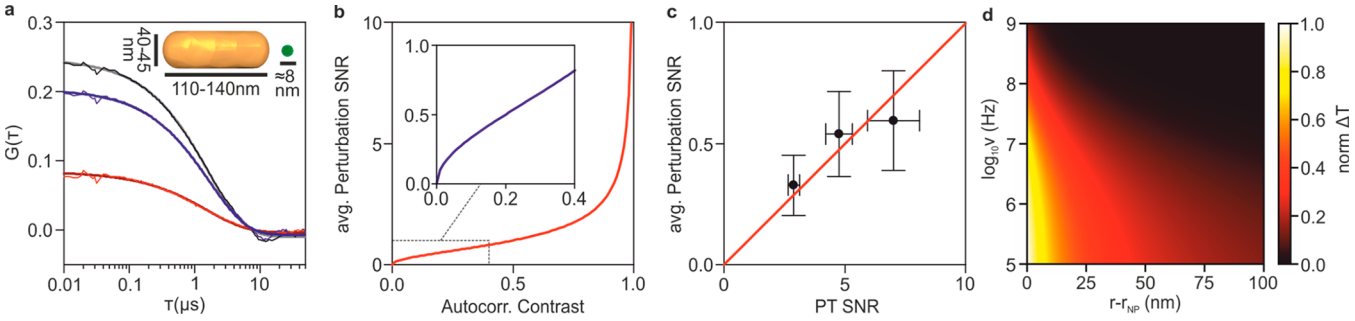

Figure 2. (a) Autocorrelations (thin lines) measured in the presence of microemulsion nanodroplets, alongside their respective stretched exponential fits (thick lines). Measurements were obtained on the same NR with constant incident polarization and different analyzer orientations. The inset shows the dimensions of the sensor NR and of the nanodroplet (analyte). (b) The relation between the average perturbation SNR and the autocorrelation contrast. The inset shows the region relevant to the experiment (a). (c) The measured average perturbation and PT SNRs (υ = 80 MHz) follow a linear relation (red line: linear fit). (d) Theoretical values of the temperature amplitude ΔT computed as a function of modulation frequency ν and of the distance from the surface of a gold sphere with a 20 nm radius.

frequency. In consequence, the change of detected intensity can be described as $\Delta P_{PT} \propto \Delta S + \Delta I$, where $\Delta I = \eta(\sqrt{R/S}\cos\phi\Delta S + 2\sqrt{SR}\Delta\cos\phi)$ denotes the change of the interference term. Our setup allows for the adjustment of linear incident (angle: α_i) and analyzed (angle: α_a) polarization as well as of the probe wavelength and, to some extent, of the Gouy phase by adjustment of the NR's position along the focal axis. We can thus tune cos ϕ as well as the ratio of S/R via the projection of the scattered field (polarized along the NR's long axis) and of the reflected field (incident polarization) on the analyzer axis. We can perform 2D-confocal scans measuring ΔP_{PT} and P_{det}, that is, scattering and PT signal, simultaneously. Figure 1b presents images of such scans performed for a set of polarization mismatch angles $\alpha_c = (\alpha_a - \alpha_i)/2$ for crossed ($\alpha_a = \alpha_i + \pi/2$) and parallel ($\alpha_a = \alpha_i$) configurations of incident versus analyzed polarizations. An example for how ΔP_{PT} and P_{det} scale with α_c ($S \gg R$, 40 nm diameter NR) is shown in Figure 1c. In both cases, we find excellent agreement with the theoretical expected values (fits). Before discussing the influence of the experimental parameters in detail, we want to demonstrate that the PT signal-to-noise ratio (SNR) indeed correlates with the SNR for analyte detection. To this aim, we compare the PT SNR with the intensity autocorrelation contrast obtained with the same NR in the presence of oil-in-water microemulsion nanodroplets.[12] These nanodroplets simulate the optical properties of ≈250 kDa proteins without the drawbacks of nonspecific sticking commonly encountered for real protein samples. Prevention of binding conserves the NR's sensing volume and ensures the comparability of results obtained at different times, while experimental parameters are varied. In the following, we compare PT SNR and autocorrelation contrast for the simplest case of a strongly scattering NR (i.e., $S \gg R$) with the incident polarization parallel to NR's long axis, the probing wavelength on the red-detuned flank of the LSPR and the NR centered in the focused probe beam. While all other parameters are kept constant, we alter the orientation of the polarization analyzer and observe the changes of the photothermal SNR and of the autocorrelation contrast $C = G(\tau = 10\ \text{ns})$. From the latter quantity, we then determine the average perturbation SNR[12] via the following relation:

$$\text{SNR}_{per} = \sqrt{\frac{C}{1-C}}$$

(compare Figure 2b). We find that both the autocorrelation contrast (see Figure 2a) and the PT-SNR decrease with an increasing difference between α_i and α_a. We further find a linear relationship between PT-SNR and SNR_{per}. This proportionality confirms that PT-spectro-microscopy can indeed be used as a means to probe the response of plasmonic structures for biodetection assays. Here we have made use of the fact that the effective extent of the modulated temperature profile around the nanoparticle depends on the modulation frequency. It scales $\propto(1/r)e^{-(r-r_{np})/\delta_\tau}$, where $\delta_\tau = \sqrt{\frac{D}{\pi\nu}}$ is the thermal attenuation length[39] and D is the surrounding medium's thermal diffusivity. This means that at low frequencies, <100 kHz, the thermal profile extends beyond the 100 nm range, whereas at ≈100 MHz, it is confined to a few tens of nanometers around the NR (compare Figure 2d). In turn, the choice of modulation frequency allows us to select how strongly thermal-lens effects, temperature changes in the near field, and the heating of the particle itself contribute to the PT signal. At low frequencies, <100 kHz, thermal-lens effects and near-field effects, as well as thermal changes of the NR's properties, are probed altogether, whereas for higher frequencies of ≈100 MHz, only thermal changes occurring in the near field and the particle will be recognized. At still higher frequencies, the response of the particle itself will dominate as the extent and amplitude of the temperature profile diminish further. Microemulsion nanodroplets are only detected in the NR's near field,[12] thus, we have chosen to perform our correlative measurements at a high modulation frequency of 80 MHz. At this frequency, δ_τ = 24 nm is close to the extent of the near field. The fast modulation therefore allows us to directly reject contributions to the PT signal from outside the NR's near-field. In order to facilitate this high-frequency modulation, we utilized a fiber-based electro-optic modulator (EOM, compare Figure 1a) that offers a ≈200 ps rise time.

We now want to better understand the influence of experimental parameters on the PT-SNR. To this aim, we perform PT measurements on NRs with similar aspect ratios but different diameters. We first want to discuss the polarization dependence of the PT-signal. While this seems trivial at first, it nonetheless will provide us with insights into the relative strengths of the contributions from ΔS, ΔI and $\Delta\cos\phi$ to ΔP_{det}. Specifically, we will focus on the case of parallel incident and analyzed polarizations ($\alpha_i = \alpha_a$). Then, only the scattered field E_s is angle-dependent and scales like $E_s(\alpha) = E_s(\alpha = 0)\cos^2\alpha$, where α is the angle between the NR's long axis and the polarizer's orientation. The PT amplitude then scales as $\Delta P_{PT}(\alpha) \propto |\Delta I\cos^2\alpha + \Delta S\cos^4\alpha|$, where ΔI and ΔS

https://doi.org/10.1021/acs.jpcc.1c07592
J. Phys. Chem. C 2021, 125, 25087−25093

are the values at $\alpha = 0$, and we can determine the relative contribution ρ of the interference term ΔI versus the pure scattering term ΔS at $\alpha = 0$ via fitting to the function: $\Delta P_{PT}(\alpha) = k|(\rho \cos^2 \alpha + (1 - |\rho|)\cos^4 \alpha)|$, where k is a constant scaling factor. If we further assume that $\eta \approx 1$ we can also determine the ratio of intensity changes due to phase shifts over changes of the scattering cross section:

$$\xi = \left| \frac{\rho}{1 - |\rho|} - \sqrt{\frac{R}{S}} \cos \phi \right| = \left| \frac{2\sqrt{SR}\Delta \cos \phi}{\Delta S} \right|$$

Note that S/R and $\cos \phi$ are obtained via the simultaneous measurement of the detected power and the subsequent fit to

$$P_{det}(\alpha)/P_{refl} \propto 1 + 2\sqrt{S/R}\eta \cos \Delta\phi \cos^2 \alpha + (S/R) \cos^4 \alpha$$

where $P_{refl} \propto R$ is measured on the glass slide next to the NR. The results of our angle-dependent PT measurements are shown in Figure 3 alongside the respective values found for S/R, $\cos \phi$, ρ, and ξ. We find that ρ is negative, which means the interference term counteracts the pure changes in scattered intensity for our confocal configuration. This is especially apparent in Figure 3b, which shows the transition from interference- to scattering-dominated PT as α approaches 0 and results in two minima of PT amplitude. We further find that, as expected for NRs with $S/R < 1$, the interference term significantly contributes to the PT signal ($|\rho| \geq 0.5$, compare Figure 3c,d). Nonetheless, the interference term is still dominated by changes in the scattering cross section ($\xi < 1$, Figure 3c) as we find that only for NRs with $S/R \ll 1$ the phase-shift-induced changes dominate ($\xi > 1$, Figure 3d). In all cases, we recognize significant PT amplitudes only for polarizations centered around the NR's long axis. From this we can conclude that we are predominantly probing the NR's response to temperature changes, and contributions to ΔP_{PT} due to scattering of light by the thermal lens itself are negligibly small in comparison.

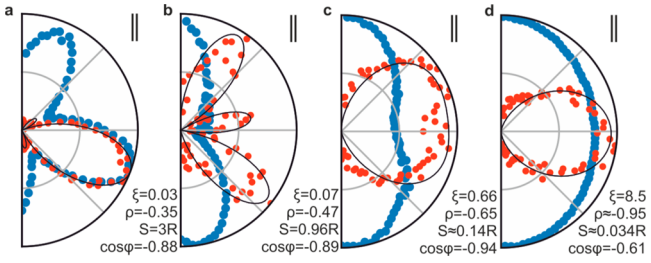

Figure 3. Parallel-angle scans in (a)−(d) depict the progression from strongly to weakly scattering NRs showing the transition from scattering- to interference-dominated PT. Black lines are fits of PT amplitude by the respective functions. PT-amplitudes (red dots) and P_{det} (blue dots) values are normalized to their maximum. All values were measured in water with $\nu = 1.1$ MHz.

We also want to test the wavelength-dependence of the PT signal. To this aim, we first take white-light scattering spectra and determine the NR's orientation by rotating both polarizers in parallel configuration. We then measure the PT response as we change the wavelength of our laser while keeping the NR positioned in the center of the focus and both polarizers aligned with the NR's long axis. Examples of such measurements performed on three NRs with different sizes are displayed in Figure 4. We find that the highest relative intensity changes ($\Delta P_{PT}/P_{det}$) for NR's with $S/R > 1$ (Figure 4 a) coincide with the highest slopes found in the corresponding white-light scattering spectrum. This is consistent with our previous finding that, in the case of $S/R > 1$, the PT signal is dominated by changes in the scattered intensity (compare also Figure 4e). Due to the limited scanning range of our laser, we unfortunately could not directly compare values on both sides of the LSPR of individual NRs. For NRs with $S/R < 1$ (Figure 4b,c) we find the highest $\Delta P_{PT}/P_{det}$ values close the LSPR frequency. This is consistent with our previous finding that, for NR's with $S/R < 1$, changes in the phase difference φ strongly contribute to the PT signal (compare Figure 4f).

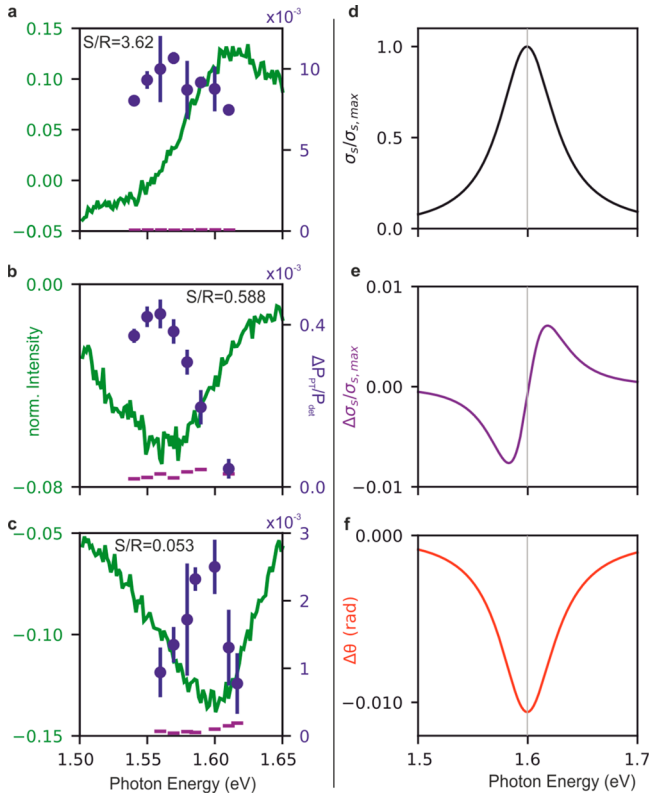

Figure 4. Left side: Photothermal spectroscopy on NRs of different sizes (40 to 10 nm diameter) decreasing from (a) to (c). Green lines are normalized white-light scattering spectra. Blue dots are relative intensity changes $\Delta P_{PT}/P_{det}$ and purple dashes indicate the noise level. Right side: Theoretical curves showing the normalized scattering cross section (d) and its relative change upon a minute reduction of the surrounding medium's dielectric constant (10^{-3}) (e), as well as the associated change of the phase difference between scattered and incident field (f).

To obtain an overview of how the PT SNR depends on the NR size, we plot the maximum $\Delta P_{PT}/P_{det}$ versus the S/R values found for multiple NR samples and normalize these values to the absorbed power (Figure 5a). The corresponding average refractive index change is computed from the temperature profile[39] in the medium surrounding the rod at distances of up to 15 nm (Figure 5b) using the thermorefractive index of water: $\frac{dn}{dt} = -8.36 \times 10^{-5}(K^{-1})$. These values reflect the absorbed power and refractive index sensitivity of the respective NRs, and we find the highest values $\Delta P_{PT}/P_{det} = 11.8 \pm 1.6$ RIU^{-1} (refractive index unit) for NRs with $S/R \approx 3$ to 5, that is, diameters of approximately 25 nm. This means an effective refractive index change on the order of 10^{-3} gives rise to intensity changes on the order of 1%. For the

https://doi.org/10.1021/acs.jpcc.1c07592
J. Phys. Chem. C 2021, 125, 25087−25093

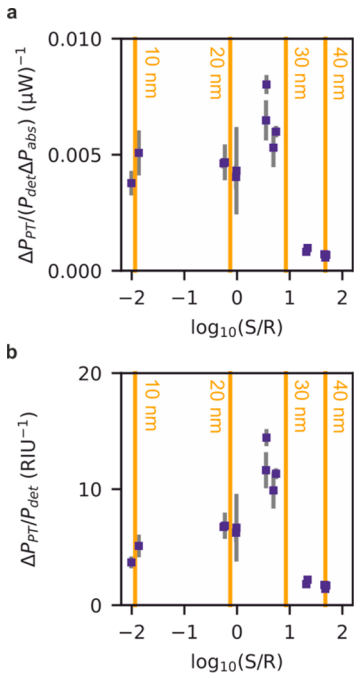

Figure 5. Comparison of maximum relative PT amplitudes $\Delta P_{PT}/P_{det}$ found for NRs with different S/R ratios (diameters indicated in yellow) after optimizing the laser wavelength and aligning the polarizers with the NR's axis. (a) Measured $\Delta P_{PT}/P_{det}$ values normalized to the absorbed power and (b) $\Delta P_{PT}/P_{det}$ normalized to the average change of refractive index units (RIU) calculated for the medium (water) inside the NR's near field (extent 15 nm).

binding of a single ≈150 kDa protein, we anticipate relative intensity changes on the same order, that is, 1 to 3%, as found by previous studies.[5,7] Single step-like changes in relative detected power on the order of 1% are detected by our system with a SNR of ≈1 at 200 MHz bandwidth. This corresponds to a SNR of ≈4500 using typical integration times of 100 ms.[7] This yields a detection limit in the range of 3 to 9 $Da(Hz)^{-1/2}$ for 0.1 mW of incident power. Our detector is not shot-noise limited and we anticipate an approximately 2-fold improvement of this figure for shot-noise limited detection. We found the maximum refractive index sensitivity for NRs with diameters of ≈25 nm. We attribute this finding to the, in comparison to larger NRs, narrower LSPR of these NRs (less volume means less radiative damping) and to a still relatively weak contribution from the interference term, which begins to significantly counteract changes in scattering cross section for NRs with $S/R \lesssim 1$ (compare Figure 3b and Figure 4b). This finding, however, has to be taken with caution as this maximum is not only a consequence of the NR dimensions but also of the experimental conditions and will differ if, for example, a different substrate-medium couple is chosen (with a higher or lower R coefficient). The conditions may be varied further for each individual NR, for example, by deviating from the parallel polarization configuration we had maintained throughout our measurements in order to compare different NR sizes. In fact, variation of polarizers orientation allows almost arbitrarily to set the effective S/R ratio for any NR via the projection of the scattered and reflected fields on the NR, with proper tuning of the analyzer axis. In theory, the highest relative changes $\Delta P_{PT}/P_{det}$ can be expected for $S \approx R$, that is, when P_{det} approaches zero as a consequence of an almost completely destructive interference between the scattered and reflected fields. This, however, also goes along with a relatively small absolute ΔP_{PT}. In turn, whether such a configuration is more desirable will depend on the assay. The desired time resolution for example imposes restrictions on the type of detector that can be used. Here we used a fast avalanche photodiode (APD) in order to detect analytes in Brownian motion with 10 ns temporal resolution (see Figure 2a). Whereas this APD has a lower noise-equivalent power than PIN-photodiodes with similar bandwidth, and is therefore advantageous for our purpose, it suffers from excess noise and is thus not shot-noise limited. In this case setting the polarizers such that $S = R$ is undesirable as the electronic detector noise already exceeds small signal amplitudes. However, in assays meant to probe slower processes, like analyte binding, single-photon-counting detectors may be more advantageous. In such a case, the high relative signal amplitudes found at $S = R$ become desirable as long as the background noise (due to undesired scattering by impurities along the optical path) is still overcome. Independently of an assay's precise nature, PT-assisted alignment may be used to find the most desirable parameters, taking into account the assay's specific restrictions and limitations by available instrumentation.

CONCLUSION

In conclusion, we have demonstrated that PT-spectromicroscopy can be used as a method for the direct optimization of nanostructure-based optoplasmonic detection assays. Specifically, we have demonstrated this optimization for the case of gold nanorods. We utilized high-frequency modulation to selectively match the thermal modulation profile to the extent of plasmonic near fields. This enabled us to show that the PT SNR scales directly with the SNR found for average perturbations caused by small nanodroplets entering and exiting a NR's near field. We have further demonstrated that PT-micro/spectroscopy helps to probe and understand the influence of various experimental parameters on the SNR. Here, we have specifically identified the best size of NRs for fast nanoplasmonic assays in a simple confocal bright-field configuration. PT-based calibration uses the refractive index change induced by photothermal heating of the sensor nanostructures themselves and is therefore, in principle, applicable to any type of optoplasmonic assay that probes changes in the dielectric environment of nanostructures.

AUTHOR INFORMATION

Corresponding Author

Michel Orrit − *Huygens-Kamerlingh Onnes Laboratory, Leiden University, 2300 RA Leiden, The Netherlands;* orcid.org/0000-0002-3607-3426; Email: orrit@physics.leidenuniv.nl

Authors

Martin. D. Baaske − *Huygens-Kamerlingh Onnes Laboratory, Leiden University, 2300 RA Leiden, The Netherlands;* orcid.org/0000-0003-2384-7557

Nasrin Asgari − *Huygens-Kamerlingh Onnes Laboratory, Leiden University, 2300 RA Leiden, The Netherlands;* orcid.org/0000-0002-9770-7605

Patrick Spaeth − *Huygens-Kamerlingh Onnes Laboratory, Leiden University, 2300 RA Leiden, The Netherlands;* orcid.org/0000-0001-8520-6216

https://doi.org/10.1021/acs.jpcc.1c07592
J. Phys. Chem. C 2021, 125, 25087−25093

Subhasis Adhikari − *Huygens-Kamerlingh Onnes Laboratory, Leiden University, 2300 RA Leiden, The Netherlands;* orcid.org/0000-0002-0914-433X

Deep Punj − *Huygens-Kamerlingh Onnes Laboratory, Leiden University, 2300 RA Leiden, The Netherlands;* orcid.org/0000-0003-3976-262X

Complete contact information is available at: https://pubs.acs.org/10.1021/acs.jpcc.1c07592

Notes

The authors declare no competing financial interest.

■ ACKNOWLEDGMENTS

This work was supported by The Netherlands Organisation for Scientific Research (NWO) and has received funding from the European Union's Horizon 2020 Research and Innovation Programme under the Marie Skłodowska-Curie Grant Agreement No. 792595 (M.D.B.).

■ REFERENCES

(1) Moerner, W. E.; Orrit, M. Illuminating Single Molecules in Condensed Matter. *Science* **1999**, *283* (5408), 1670−1676.
(2) Gaiduk, A.; Yorulmaz, M.; Ruijgrok, P. V.; Orrit, M. Room-Temperature Detection of a Single Molecule's Absorption by Photothermal Contrast. *Science* **2010**, *330* (6002), 353−356.
(3) Kukura, P.; Celebrano, M.; Renn, A.; Sandoghdar, V. Imaging a Single Quantum Dot When It Is Dark. *Nano Lett.* **2009**, *9* (3), 926−929.
(4) Ament, I.; Prasad, J.; Henkel, A.; Schmachtel, S.; Sönnichsen, C. Single Unlabeled Protein Detection on Individual Plasmonic Nanoparticles. *Nano Lett.* **2012**, *12* (2), 1092−1095.
(5) Zijlstra, P.; Paulo, P. M. R.; Orrit, M. Optical Detection of Single Non-Absorbing Molecules Using the Surface Plasmon Resonance of a Gold Nanorod. *Nat. Nanotechnol.* **2012**, *7* (6), 379−382.
(6) Rosman, C.; Prasad, J.; Neiser, A.; Henkel, A.; Edgar, J.; Sönnichsen, C. Multiplexed Plasmon Sensor for Rapid Label-Free Analyte Detection. *Nano Lett.* **2013**, *13* (7), 3243−3247.
(7) Beuwer, M. A.; Prins, M. W. J.; Zijlstra, P. Stochastic Protein Interactions Monitored by Hundreds of Single-Molecule Plasmonic Biosensors. *Nano Lett.* **2015**, *15* (5), 3507−3511.
(8) Wulf, V.; Knoch, F.; Speck, T.; Sönnichsen, C. Gold Nanorods as Plasmonic Sensors for Particle Diffusion. *J. Phys. Chem. Lett.* **2016**, *7* (23), 4951−4955.
(9) Taylor, A. B.; Zijlstra, P. Single-Molecule Plasmon Sensing: Current Status and Future Prospects. *ACS Sensors* **2017**, *2* (8), 1103−1122.
(10) Verschueren, D. V.; Pud, S.; Shi, X.; De Angelis, L.; Kuipers, L.; Dekker, C. Label-Free Optical Detection of DNA Translocations through Plasmonic Nanopores. *ACS Nano* **2019**, *13* (1), 61−70.
(11) Zhang, P.; Ma, G.; Dong, W.; Wan, Z.; Wang, S.; Tao, N. Plasmonic Scattering Imaging of Single Proteins and Binding Kinetics. *Nat. Methods* **2020**, *17* (10), 1010−1017.
(12) Baaske, M. D.; Neu, P. S.; Orrit, M. Label-Free Plasmonic Detection of Untethered Nanometer-Sized Brownian Particles. *ACS Nano* **2020**, *14* (10), 14212−14218.
(13) Foreman, M. R.; Swaim, J. D.; Vollmer, F. Whispering Gallery Mode Sensors. *Adv. Opt. Photonics* **2015**, *7* (2), 168.
(14) Kim, E.; Baaske, M. D.; Vollmer, F. Towards Next-Generation Label-Free Biosensors: Recent Advances in Whispering Gallery Mode Sensors. *Lab Chip* **2017**, *17* (7), 1190−1205.
(15) Dantham, V. R.; Holler, S.; Barbre, C.; Keng, D.; Kolchenko, V.; Arnold, S. Label-Free Detection of Single Protein Using a Nanoplasmonic-Photonic Hybrid Microcavity. *Nano Lett.* **2013**, *13* (7), 3347−3351.
(16) Baaske, M. D.; Foreman, M. R.; Vollmer, F. Single-Molecule Nucleic Acid Interactions Monitored on a Label-Free Microcavity Biosensor Platform. *Nat. Nanotechnol.* **2014**, *9* (11), 933−939.
(17) Baaske, M. D.; Vollmer, F. Optical Observation of Single Atomic Ions Interacting with Plasmonic Nanorods in Aqueous Solution. *Nat. Photonics* **2016**, *10* (11), 733−739.
(18) Kim, E.; Baaske, M. D.; Vollmer, F. In Situ Observation of Single-Molecule Surface Reactions from Low to High Affinities. *Adv. Mater.* **2016**, *28* (45), 9941−9948.
(19) Heylman, K. D.; Thakkar, N.; Horak, E. H.; Quillin, S. C.; Cherqui, C.; Knapper, K. A.; Masiello, D. J.; Goldsmith, R. H. Optical Microresonators as Single-Particle Absorption Spectrometers. *Nat. Photonics* **2016**, *10* (12), 788−795.
(20) Kim, E.; Baaske, M. D.; Schuldes, I.; Wilsch, P. S.; Vollmer, F. Label-Free Optical Detection of Single Enzyme-Reactant Reactions and Associated Conformational Changes. *Sci. Adv.* **2017**, *3* (3), e1603044.
(21) Hogan, L. T.; Horak, E. H.; Ward, J. M.; Knapper, K. A.; Nic Chormaic, S.; Goldsmith, R. H. Toward Real-Time Monitoring and Control of Single Nanoparticle Properties with a Microbubble Resonator Spectrometer. *ACS Nano* **2019**, *13* (11), 12743−12757.
(22) Taylor, R. W.; Mahmoodabadi, R. G.; Rauschenberger, V.; Giessl, A.; Schambony, A.; Sandoghdar, V. Interferometric Scattering Microscopy Reveals Microsecond Nanoscopic Protein Motion on a Live Cell Membrane. *Nat. Photonics* **2019**, *13* (7), 480−487.
(23) Bujak, Ł.; Holanová, K.; García Marín, A.; Henrichs, V.; Barvík, I.; Braun, M.; Lánský, Z.; Piliarik, M. Fast Leaps between Millisecond Confinements Govern Ase1 Diffusion along Microtubules. *Small Methods* **2021**, *5*, 2100370.
(24) Cohen, A. E.; Moerner, W. E. Suppressing Brownian Motion of Individual Biomolecules in Solution. *Proc. Natl. Acad. Sci. U. S. A.* **2006**, *103* (12), 4362−4365.
(25) Tong, L.; Miljković, V. D.; Käll, M. Alignment, Rotation, and Spinning of Single Plasmonic Nanoparticles and Nanowires Using Polarization Dependent Optical Forces. *Nano Lett.* **2010**, *10* (1), 268−273.
(26) Krishnan, M.; Mojarad, N.; Kukura, P.; Sandoghdar, V. Geometry-Induced Electrostatic Trapping of Nanometric Objects in a Fluid. *Nature* **2010**, *467* (7316), 692−695.
(27) Ruijgrok, P. V.; Verhart, N. R.; Zijlstra, P.; Tchebotareva, A. L.; Orrit, M. Brownian Fluctuations and Heating of an Optically Aligned Gold Nanorod. *Phys. Rev. Lett.* **2011**, *107* (3), 037401.
(28) Braun, M.; Würger, A.; Cichos, F. Trapping of Single Nano-Objects in Dynamic Temperature Fields. *Phys. Chem. Chem. Phys.* **2014**, *16* (29), 15207−15213.
(29) Squires, A. H.; Lavania, A. A.; Dahlberg, P. D.; Moerner, W. E. Interferometric Scattering Enables Fluorescence-Free Electrokinetic Trapping of Single Nanoparticles in Free Solution. *Nano Lett.* **2019**, *19* (6), 4112−4117.
(30) Harada, M.; Iwamoto, K.; Kitamori, T.; Sawada, T. Photothermal Microscopy with Excitation and Probe Beams Coaxial under the Microscope and Its Application to Microparticle Analysis. *Anal. Chem.* **1993**, *65* (20), 2938−2940.
(31) Mawatari, K.; Kitamori, T.; Sawada, T. Individual Detection of Single-Nanometer-Sized Particles in Liquid by Photothermal Microscope. *Anal. Chem.* **1998**, *70* (23), 5037−5041.
(32) Boyer, D.; Tamarat, P.; Maali, A.; Lounis, B.; Orrit, M. Photothermal Imaging of Nanometer-Sized Metal Particles Among Scatterers. *Science (Washington, DC, U. S.)* **2002**, *297* (5584), 1160−1163.
(33) Berciaud, S.; Cognet, L.; Poulin, P.; Weisman, R. B.; Lounis, B. Absorption Spectroscopy of Individual Single-Walled Carbon Nanotubes. *Nano Lett.* **2007**, *7* (5), 1203−1207.
(34) Gaiduk, A.; Ruijgrok, P. V.; Yorulmaz, M.; Orrit, M. Detection Limits in Photothermal Microscopy. *Chem. Sci.* **2010**, *1* (3), 343.
(35) Spaeth, P.; Adhikari, S.; Le, L.; Jollans, T.; Pud, S.; Albrecht, W.; Bauer, T.; Caldarola, M.; Kuipers, L.; Orrit, M. Circular Dichroism Measurement of Single Metal Nanoparticles Using Photothermal Imaging. *Nano Lett.* **2019**, *19* (12), 8934−8940.

(36) Adhikari, S.; Spaeth, P.; Kar, A.; Baaske, M. D.; Khatua, S.; Orrit, M. Photothermal Microscopy: Imaging the Optical Absorption of Single Nanoparticles and Single Molecules. *ACS Nano* **2020**, *14* (12), 16414−16445.
(37) Selmke, M.; Braun, M.; Cichos, F. Photothermal Single-Particle Microscopy: Detection of a Nanolens. *ACS Nano* **2012**, *6* (3), 2741−2749.
(38) Chen, C.; Shimizu, H.; Kitamori, T. Review of Ultrasensitive Readout for Micro-/Nanofluidic Devices by Thermal Lens Microscopy. *J. Opt. Microsystems* **2021**, *1* (02), 035001−035007.
(39) Baffou, G. *Thermoplasmonics*; Cambridge University Press, 2017, DOI: 10.1017/9781108289801.

https://doi.org/10.1021/acs.jpcc.1c07592
J. Phys. Chem. C 2021, 125, 25087−25093